communications biology

A Nature Portfolio journal

Article

https://doi.org/10.1038/s42003-025-08218-1

Structure of MICU from non-metazoan *Dictyostelium discoideum* reveals unique characteristics

Minwoo Jin[1,2], Jihyeong Yang[1,2], Jongseo Park[1,2,4], Hyunwoo Kim[1,2] & Soo Hyun Eom[1,2,3]

In most eukaryotes, the mitochondrial calcium uniporter (MCU) mediates Ca^{2+} influx into the mitochondrial matrix through a process regulated by MICUs and the EMRE. In *Dictyostelium discoideum*, a model organism for amoebozoans that lack an EMRE, the MCU complex consists solely of the MCU and MICU. Most likely, therefore, the mechanism by which *Dd*MICU regulates the *Dd*MCU differs from the extensively studied metazoan MCU-EMRE-MICU system. Here, we report the crystal structure of Ca^{2+}-bound *Dd*MICU at 2.5 Å resolution. Unlike human MICUs, which contain two Ca^{2+}-binding EF-hand motifs, *Dd*MICU possesses three EF-hand motifs, each with a submicromolar Ca^{2+} binding affinity. The overall structure of *Dd*MICU is comparable to that of human MICUs, and their well-conserved dimer interface interactions are similar. In addition to the face-to-face dimer observed in human MICUs, *Dd*MICU forms a head-to-head dimer with multimeric states that equilibrate between tetrameric and dimeric forms, depending on the solution ionic strength. Moreover, the C-helix of *Dd*MICU plays a critical role in membrane binding. These findings provide a molecular basis for the unique mechanism regulating Ca^{2+} uptake by MICUs in an EMRE-free system and offer insight into the evolution and functional diversity of the MCU complex in non-metazoan organisms.

Mitochondrial Ca^{2+} homeostasis is crucial for a variety of cellular processes, including energy metabolism, necrosis, apoptosis, and intracellular and intercellular signaling[1–3]. Impairment of mitochondrial Ca^{2+} homeostasis can lead to neurodegenerative disease, cardiovascular disease, hypertension, cancer, and diabetes[4,5]. Several ion channels and transporters, including voltage-dependent anion-selective channels (VDACs), Na^{+}/Ca^{2+} exchangers (NCLX), leucine zipper EF-hand containing transmembrane protein 1 (LETM1), and the mitochondrial calcium uniporter (MCU) complex, precisely regulate mitochondrial Ca^{2+} homeostasis[6,7]. The MCU complex is a highly selective Ca^{2+} uptake channel complex in vertebrates, which includes the pore-forming MCU, its paralog (MCUb), essential MCU regulator (EMRE), MCU regulator 1 (MCUR1), and several mitochondrial Ca^{2+} uptake proteins (MICU1, MICU2, MICU3, and MICU1.1)[8–16]. The MICUs, which are localized within the mitochondrial intermembrane space, regulate Ca^{2+} uptake by the MCU through Ca^{2+} binding via their EF-hand motifs[14,17].

In humans, MICUs include three paralogs and one splicing variant (*Hs*MICU1, *Hs*MICU2, *Hs*MICU3, and *Hs*MICU1.1), and the Ca^{2+} uptake threshold for the MCU complex in different tissues is dependent on the expression level of the MICUs[15–17]. In its Ca^{2+}-free state, MICU1 acts as a gatekeeper by setting the Ca^{2+} uptake threshold of the MCU complex, while in the Ca^{2+}-bound state it acts as an activator by potentiating Ca^{2+} uptake[18,19]. The molecular structure of MICU1 is a hexamer in the Ca^{2+}-free state and a dimer in the Ca^{2+}-bound state[20]. MICU2, which interacts with MICU1, increases the Ca^{2+} uptake threshold of the MCU complex and exhibits lower affinity for Ca^{2+} than the MICU1 homodimer[17,21,22]. MICU3 is primarily expressed in the central nervous system and skeletal muscle and also interacts with MICU1 but as an activator of the MCU complex[15,23–26]. MICU2 and MICU3 form a back-to-back (B-B) heterodimer in the Ca^{2+}-free state and a face-to-face (F-F) heterodimer in the Ca^{2+}-bound state[27,28] (Supplementary Fig. 1). The MICU1-MICU2 F-F heterodimer can form a linear dimer of heterodimers through B-B dimer interaction between MICU2 proteins[29]. Notably, a dimer of the MICU1-MICU2 heterodimer was observed in an O-shaped MCU holocomplex (dimer of MCU-EMRE tetramer with a dimer of the MICU1-MICU2 heterodimer) in cryo-EM

[1]School of Life Sciences, Gwangju Institute of Science and Technology (GIST), Gwangju, Republic of Korea. [2]Steitz Center for Structural Biology, Gwangju Institute of Science and Technology (GIST), Gwangju, Republic of Korea. [3]Department of Chemistry, Gwangju Institute of Science and Technology (GIST), Gwangju, Republic of Korea. [4]Present address: Obesity & Metabolic Research Team, Hanmi Pharmaceutical, R&D Center, Dongtangiheung-ro, Hwaseong-si, Gyeonggi-do, Republic of Korea. e-mail: eom@gist.ac.kr

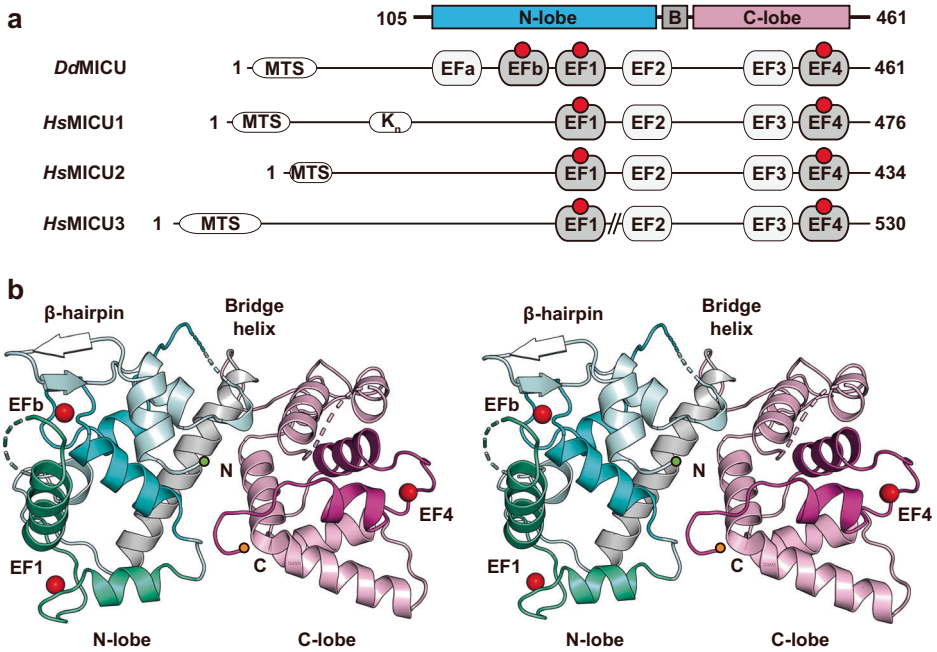

Fig. 1 | Overall structure of the *Dd*MICU. **a** Schematic representation of *Dd*MICU and human MICUs: MTS, mitochondrial targeting sequence; K_n, poly lysine; EF, EF-hand motif; B, bridge helix. The N-lobe, bridge helix and C-lobe are colored cyan, dark gray and pink, respectively. The Ca^{2+}-binding canonical EF-hand motifs are highlighted in gray and marked with a red circle. The slashed area in *Hs*MICU3 indicates an omission of 40 amino acids. **b** Stereo view of the cartoon representation of the *Dd*MICU monomer structure. Missing regions are depicted with dotted ribbons. The Ca^{2+} bound in *Dd*MICU is shown as a red sphere, and the N-lobe, bridge helix and C-lobe are colored greenish, grayish and pinkish, respectively.

structures[30–32]. This suggests the MCU gating mechanism is regulated via Ca^{2+}-dependent pore blocking by MICUs.

In metazoans, MICU1 and the EMRE are the major regulatory proteins controlling Ca^{2+} uptake into the mitochondrial matrix and interact directly with the MCU complex[30,31]. MICU1 interacts with the DXXE motif of the MCU in a Ca^{2+}-dependent manner to control the opening and closing of the MCU, thereby regulating cellular metabolism and survival[33–35]. Expression of MICU1 in 138 sequenced eukaryotes, excluding fungi, has co-evolved with the MCU[36,37]. By contrast, the EMRE is highly conserved exclusively in metazoan MCU complexes, even though it plays an essential role in linking MICU1 to the MCU and activating Ca^{2+} uptake[12,38,39]. *Dictyostelium discoideum* serves as a minimal eukaryotic model for studying the MCU complex, as it possesses only a single MCU (*Dd*MCU) and MICU (*Dd*MICU)[40]. Unlike in metazoans, Ca^{2+} uptake by *Dd*MCU is activated without the EMRE[38,40], and cardiolipin plays an essential role in the process[41]. While the conformation of the N-terminal domain in *Dd*MCU is entirely different from that in the human MCU, the Ca^{2+}-dependent destabilization of oligomerization is similar[42]. Although structural and functional studies of the *Dd*MCU N-terminal domain have been conducted[42], a full understanding of the mechanism governing the *Dd*MCU complex requires detailed structural and biochemical information on *Dd*MICU, the sole regulatory protein in the *Dd*MCU complex.

Here, we determined the crystal structure of Ca^{2+}-bound *Dd*MICU at 2.5 Å, which revealed that *Dd*MICU consists of two lobes (N-lobe and C-lobe) and binds three Ca^{2+} ions via canonical EF-hand motifs (EFb, EF1, EF4). The Ca^{2+} binding affinity of these motifs was in the submicromolar range, as with *Hs*MICU1. Structurally, *Dd*MICU is comparable to human MICUs, with an additional Ca^{2+} binding site in the EFb motif. Like human MICUs, *Dd*MICU forms a F-F dimer via conserved interface interactions but also adopts a head-to-head (H-H) dimer conformation. *Dd*MICU exists in an equilibrium state between dimeric and tetrameric forms and can bind liposomes when the C-terminal helix is present. In our study, by combining the crystal structure of a Ca^{2+}-bound *Dd*MICU with biochemical analyses, we uncovered the molecular basis for the unique role of *Dd*MICU in a MCU system lacking EMRE.

Results

Overall structure of *Dd*MICU

We purified *Dd*MICU (residues 105–461) and used it for crystallization and biochemical studies (Fig. 1a). Endeavoring to crystallize the *Dd*MICU in Ca^{2+}-bound and unbound states, we obtained diffraction-quality crystals in its Ca^{2+}-bound state. The crystal structure of Ca^{2+}-bound *Dd*MICU was then determined by combining the molecular replacement method with single-wavelength anomalous diffraction (MR-SAD) phasing at 2.5 Å resolution with R_{work} and R_{free} values of 22.1% and 26.0%, respectively (Table 1). The asymmetric unit (ASU) consisted of a *Dd*MICU dimer, and the overall structure of *Dd*MICU comprised two lobes (N-lobe and C-lobe) connected by a bridge helix (Fig. 1b). The N-lobe contained two canonical EF-hand motifs (EFb and EF1) while the C-lobe contained one (EF4), and each of the three motifs was paired with an EF-hand-like motif (EFa, EF2, EF3).

The EFb motif, which was first noticed in MICUs from plants, is not conserved in mammalian MICUs[43]. To determine whether the EFb motif is specific to plants or is also present in the protist *Dictyostelium*, we assessed the protein domain compositions of 650 MICU proteins in three eukaryotic groups: metazoans, protists and plants (Supplementary Data 1). With the exception of *Caenorhabditis* species, metazoan MICUs were predicted to be unable to bind Ca^{2+} to the EFb motif, while protists and plant MICUs were predicted to bind Ca^{2+} to the EFb motif. Subsequent alignment of selected MICU sequences representing each group with *Dd*MICU showed the sequence diversity of the EF-hand motifs in MICUs (Supplementary Fig. 2). The canonical EF-hand sequence (X, Y, Z, −Y, and −Z position carboxyl or carbonyl residues) of the EF1 and EF4 motifs was conserved throughout the entire sample (Fig. 2a, Supplementary Fig. 2) and was also conserved in the EFb motif in non-metazoan MICUs. However, the EFb motif in metazoan MICUs lacked the aspartate residues at the X, Y and Z positions needed for Ca^{2+} binding.

Ca^{2+} ions bound to the three EF-hand motifs in *Dd*MICU through pentagonal bi-pyramidal coordination geometry, which is the typical Ca^{2+} coordination in canonical EF-hand motifs (Fig. 2a). To compare the Ca^{2+} binding properties of each EF-hand in *Dd*MICU with *Hs*MICU1, we measured the Ca^{2+} binding affinity of EF-hand double mutants (*Dd*MICU^{EFb}, *Dd*MICU^{EF1}, and *Dd*MICU^{EF4}) in which only one of the three EF-hand motifs could bind Ca^{2+}. The K_d values for Ca^{2+} binding to EFb, EF1 and EF4 were 0.36 ± 0.03 μM, 0.36 ± 0.03 μM and 0.24 ± 0.02 μM, respectively (Fig. 2b), which are similar to the apparent Ca^{2+} binding affinities in *Hs*MICU1 (0.29 ± 0.01 μM in EF1, 0.37 ± 0.15 μM in EF4)[22]. Additionally, like *Hs*MICU1 and *Hs*MICU2, *Dd*MICU exhibited significant stabilization upon Ca^{2+} binding to each EF-hand (Supplementary Fig. 3). The melting temperature (T_m) of *Dd*MICU in the apo state (38.4 ± 0.1 °C) was

Table 1 | Data collection and refinement statistics

	*Dd*MICU (PDB: 9K6M)	*Dd*MICU SeMet
Data collection		
Space group	$I4_122$	$I4_122$
Cell dimensions		
a, *b*, *c* (Å)	103.9, 103.9, 297.5	104.5, 104.5, 295.0
α, β, γ (°)	90.0, 90.0, 90.0	90.0, 90.0, 90.0
Resolution (Å)	49.6–2.5 (2.60–2.50)	50.0–3.5 (3.56–3.50)
R_{merge}[a]	19.3 (62.3)	28.3 (89.9)
$CC_{1/2}$	0.998 (0.815)	0.991 (0.927)
$I / \sigma I$	18.5 (5.2)	29.1 (8.1)
Completeness (%)	99.9 (100.0)	99.9 (100.0)
Redundancy	25.4 (20.8)	24.6 (23.9)
Refinement		
Resolution (Å)	49.1–2.5	
No. unique reflections	28,114 (2816)	
R_{work}/R_{free}[b] (%)	22.1/26.0	
No. atoms		
Protein	4214	
Ligand/ion	6	
Water	78	
B-factors		
Protein	44.9	
Ligand/ion	40.0	
Water	34.2	
R.m.s. deviations		
Bond lengths (Å)	0.009	
Bond angles (°)	1.40	
Ramachandran plot (%)		
Favored/allowed/disallowed	96.2/3.8/0.0	

Values in parentheses are for the highest resolution shell.
[a]$R_{merge} = \sum_h \sum_i | I(h)_i - \langle I(h) \rangle | / [\sum_h \sum_i I(h)_i]$, where $I(h)$ is the intensity of reflection of h, $\sum_h$ is the sum over all reflections and $\sum_i$ is the sum over i measurements of reflection h.
[b]$R_{work} = \sum_{hkl} ||F_o| - |F_c|| / (\sum_{hkl} |F_o|)$; 5% of the reflections were excluded for the R_{free} calculation.

comparable to that of *Hs*MICU1 (40 °C). In the Ca^{2+}-bound state, however, the T_m of *Dd*MICU (76.6 ± 0.3 °C) was significantly higher than that of *Hs*MICU1 or *Hs*MICU2 (*Hs*MICU1; 55 °C, *Hs*MICU2; 63 °C)[22]. The T_m of the EFb single mutant (T_m of 57.8 ± 0.1 °C), which binds Ca^{2+} at EF1 and EF4, was similar to that of *Hs*MICU1 and *Hs*MICU2, suggesting that Ca^{2+} binding to the EFb motif further stabilizes the *Dd*MICU. Human MICUs are stabilized by Ca^{2+} binding and set the Ca^{2+} uptake threshold of the MCU complex based on a Ca^{2+} binding affinity of about 0.3 μM. Given the present results, *Dd*MICU would be expected to set a threshold for the *Dd*MCU complex based on a similar Ca^{2+} binding affinity, and the EFb motif may help maintain the activation state of the *Dd*MCU complex by stabilizing the Ca^{2+}-bound state conformation of the *Dd*MICU.

Comparisons of the *Dd*MICU structure with *Hs*MICUs

To assess structural differences, the Ca^{2+}-bound *Dd*MICU monomer and human MICU monomers were aligned and the root mean square deviation (RMSD) values were calculated (Table 2). The RMSDs between the *Dd*MICU and human MICU monomers were approximately 3.0 Å. The RMSDs between the C-lobes were 1.7 Å or less, and between the N-lobes were 2.1 Å or more. We next compared the *Dd*MICU structure with *Hs*MICU1 in the *Hs*MICU1-*Hs*MICU2 dimer, which had the highest sequence homology with *Dd*MICU among human MICUs and was a physiologically relevant formation (Fig. 3a). When we superimposed the *Dd*MICU and *Hs*MICU1 based on the C-lobe, the N-lobe of the *Dd*MICU was rotated outward by approximately 20° (Fig. 3b).

To make a more detailed comparison, we separately superimposed the N- and C-lobes of *Dd*MICU on corresponding lobes of *Hs*MICU1. The N-lobe, which bound an additional Ca^{2+} in the EFb motif, differed somewhat from the N-lobe in humans (Fig. 3c). The EF-like motif of *Hs*MICU1, which was aligned to the EFb motif of *Dd*MICU, was loosened, and the α3-helix was located approximately 10 Å away. Notably, the hydrophobic patch at the α2, α4 and bridge helices interacted with phenylalanine residues in *Hs*MICU1, which are conserved among *Hs*MICUs (*Hs*MICU1; Phe195, *Hs*MICU2; Phe228, and *Hs*MICU3; Phe209) (Fig. 3d). However, the canonical EF-hand loop in the EFb motif in *Dd*MICU was fixed by Ca^{2+} binding to Asp191, and Phe187 interacted with Val153 on the exterior but not with the hydrophobic patch interior. The phenyl group of Phe187 was rotated about 120° in comparison to that residue in human MICUs. Simultaneously, the α7-helix of *Dd*MICU was a turn shorter than in human MICUs due to the structural hindrance of the EFb motif. When we compared the C-lobe structure, it differed slightly from *Hs*MICU1 in that the α11-helix of *Dd*MICU was straight, whereas it had a short break caused by kink in *Hs*MICU1 (Fig. 3e). Moreover, the α11-helices in *Hs*MICUs in the Ca^{2+}-bound state were all kinked or shortened. Taken together, these results show the overall structure of *Dd*MICU to be similar to that of *Hs*MICUs, though there are local differences.

Structural details in the F-F dimer interface of *Dd*MICU

MICU F-F dimers are known to function as gatekeepers within the MCU complex, and their structure is common to all known MICUs[20,27–32,44,45] (Supplementary Fig. 4). The F-F dimer in *Dd*MICU, observed through crystallographic symmetry, was similar to that in *Hs*MICUs other than *Hs*MICU1 in the Ca^{2+}-bound state, with a RMSD value of about 3.2 Å (Fig. 4a, Table 2). Despite a sequence homology of about 50% between *Dd*MICU and *Hs*MICU1, the RMSD between homodimers of *Dd*MICU and *Hs*MICU1 was high, about 13.6 Å (Supplementary Fig. 5, Table 2). Consistent with the RMSD values, the interface area of the F-F dimer for *Dd*MICU (1370 $Å^2$) was similar to those of F-F dimers of *Hs*MICU1-*Hs*MICU2, *Hs*MICU2 or *Hs*MICU3 (1400 $Å^2$), but not in *Hs*MICU1 (470 $Å^2$) (Table 3 and Fig. 4b). Moreover, the calculated binding energy of the *Dd*MICU F-F dimer (−10.6 kcal/mol) was comparable to that of the F-F dimers of *Hs*MICU1-*Hs*MICU2, *Hs*MICU2 or *Hs*MICU3 (−9.0 kcal/mol), but not *Hs*MICU1 (−6.6 kcal/mol). When we assessed the sequence conservation on the surface of *Dd*MICU, it clearly matched all the F-F dimer interface residues, which were highly conserved with conservation scores over 70% in the ConSurf server (Fig. 4c). We therefore suggest that the F-F dimer of *Dd*MICU has a similar overall topology to *Hs*MICU1-*Hs*MICU2 and to the *Hs*MICU2 and *Hs*MICU3 dimers, reflecting a conserved dimer interface with a similar interface area and calculated binding energy.

We next compared the interacting residues at the F-F dimer interface to confirm whether the essential interactions for dimerization in *Hs*MICU1-*Hs*MICU2 were conserved in *Dd*MICU. With *Dd*MICU, the F-F dimer interface interactions involved three pairs of electrostatic interactions (A: Ser216-Asp369, B: Lys222-Tyr391 and C: Tyr435-Asp375) as well as hydrophobic interactions (Fig. 4d). Notably, the interaction between Ser216 and Asp369 was conserved in *Hs*MICU1-*Hs*MICU2, where it corresponded to an Arg221(*Hs*MICU1)-Asp330(*Hs*MICU2) interaction, which is an important salt bridge at interface I in *Hs*MICU1-*Hs*MICU2[29] (Fig. 4e). Additionally, the hydrogen bond with Tyr391 was conserved with Arg352(*Hs*MICU2) and was essential for heterodimerization at interface I in *Hs*MICU1-*Hs*MICU2[28,30]. These two electrostatic interactions were not conserved at interface II in *Hs*MICU1-*Hs*MICU2 (Fig. 4f). Interestingly, Tyr435 and Asp375 formed a hydrogen bond through the side chain hydroxyl and carboxyl groups, and these interacting residues were conserved in *Dictyostelium* species. Thus, the electrostatic interactions in the *Dd*MICU F-F dimer includes two hydrogen bonds that are similar to those observed in *Hs*MICUs and one putative *Dictyostelium*-specific hydrogen bond.

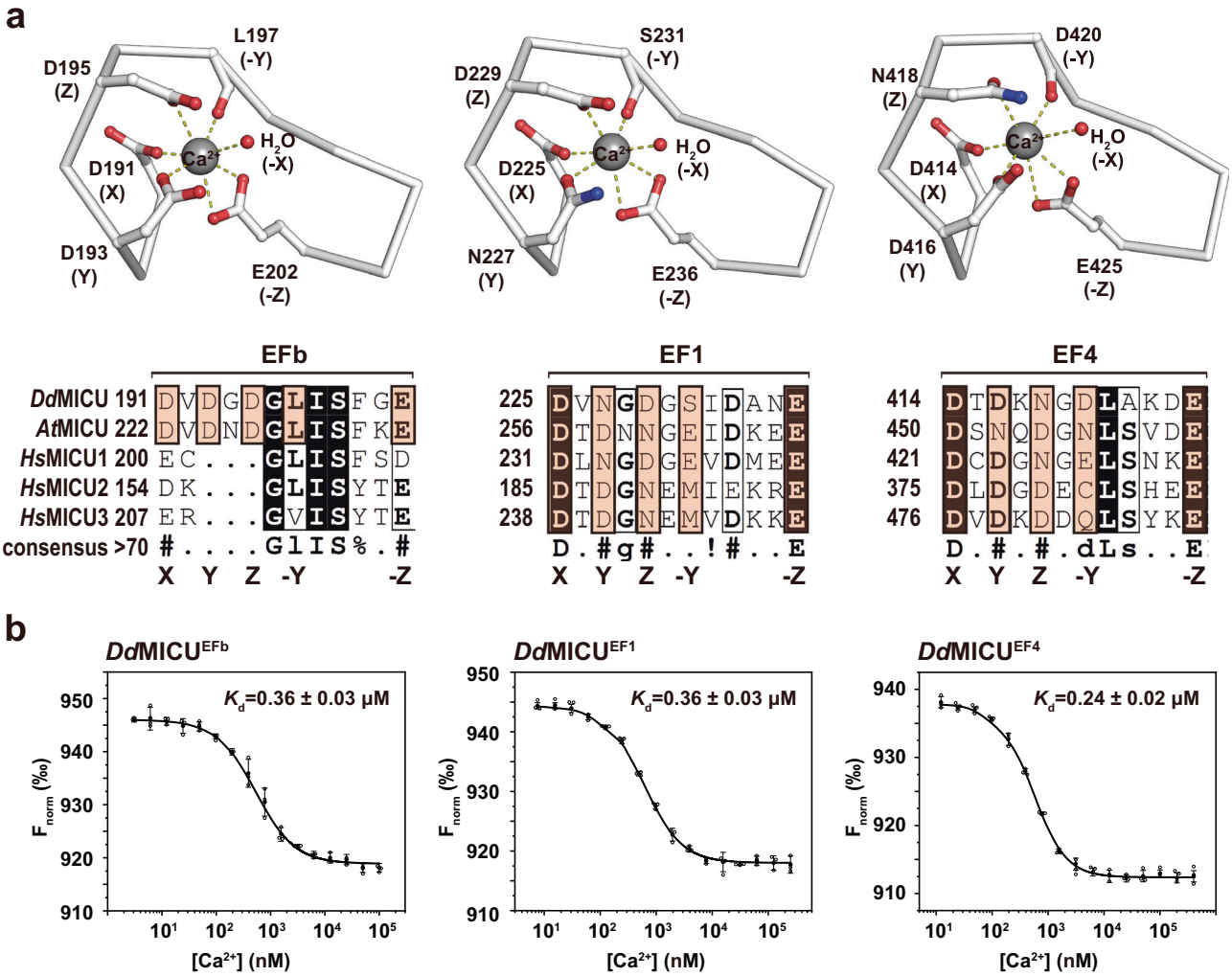

Fig. 2 | Ca^{2+}-binding EF-hand motifs in the *Dd*MICU. a Cartoon representation of the Ca^{2+} coordination geometry in the canonical EF-hand motifs of *Dd*MICU. The gray and red spheres represent Ca^{2+} and water molecules, respectively. The Ca^{2+} coordinating residues are shown as ball-and-sticks, and interactions are depicted as yellow dotted lines. Below, multiple sequence alignments of EF-hand sequences are shown, with canonical EF-hand motif sequences indicated in salmon. **b** Dose response curves for Ca^{2+} binding to *Dd*MICU EF-hand mutants, plotting normalized fluorescence against Ca^{2+} concentration. All experiments are done in triplicate; the circle and error bar indicate the mean and standard deviation. The calculated K_d value from each binding curve is shown at the upper right.

Table 2 | RMSD values between *Dd*MICU and human MICU structures

Protein		*Hs*MICU1	*Hs*MICU2	*Hs*MICU3	*Hs*MICU1-2 (MICU1)	*Hs*MICU1-2 (MICU2)
RMSD (Å)	F-F dimer	13.6	2.8	3.2	3.2	
	Monomer	3.0	2.6	3.0	2.9	3.2
	N-lobe	2.5	2.6	2.5	2.1	2.9
	C-lobe	1.3	1.4	1.7	1.6	1.6
Sequence Homology (%)		50	45	41	–	

In addition to the electrostatic interactions at the F-F dimer interface in *Dd*MICU, we analyzed the hydrophobic interactions using the PDBePISA server. Based on the calculated solvation energies, which correspond to hydrophobic interactions, four I/L knob residues (Ile219, Ile223, Leu372, and Leu376) were the primary contributors to the hydrophobic interactions at the F-F dimer interface of *Dd*MICU (Fig. 4d). The solvation energies of these four I/L knob residues were the highest among 21 hydrophobic interaction residues, with $\Delta^{i}G$ values of 1.34, 1.79, 1.59 and 1.60, respectively. Leu372 and Leu376 in the α11-helix interacted with the hydrophobic cleft formed by the α4-helix and α5-helix, and Ile219 and Ile223 in the α5-helix interacted with the hydrophobic cleft formed by the α11-helix and α12-helix. Notably, Ile223 and Leu376 were conserved as methionine knobs in the *Hs*MICU1-*Hs*MICU2 structure and were similarly positioned within the hydrophobic pocket formed by opposing EF-hand helices[29] (Fig. 4e). Ile223 and Leu372 also interacted with Tyr391 and Tyr435, which participated in electrostatic interactions. Collectively then, the F-F dimer structure of *Dd*MICU is similar to that of human MICUs, and the electrostatic and hydrophobic interactions at the F-F dimer interface observed in human MICUs are well conserved in *Dd*MICU.

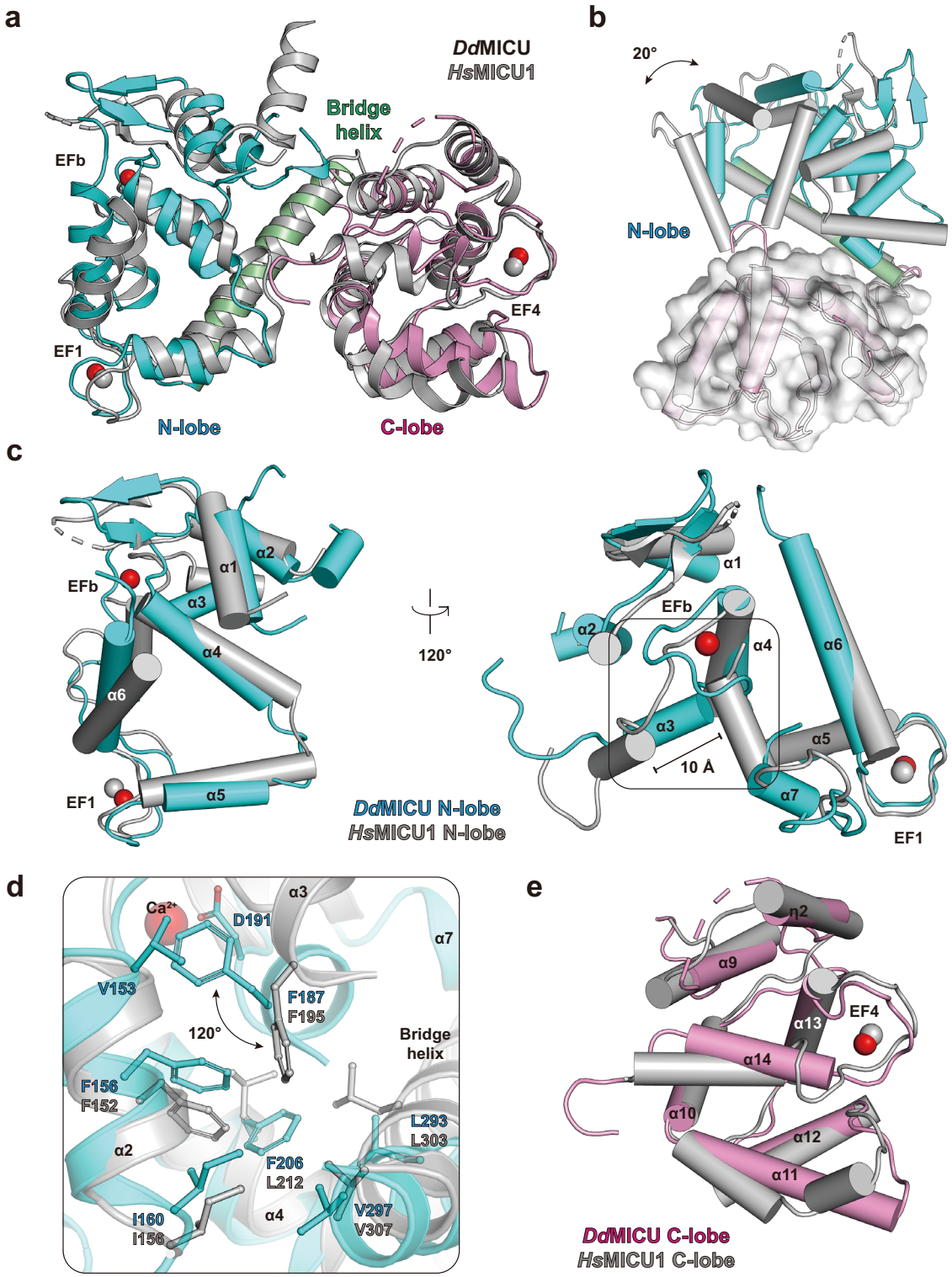

Fig. 3 | Structural comparison of *Dd*MICU and *Hs*MICU1. a Cartoon representation of the superimposed *Dd*MICU and *Hs*MICU1 (PDB code: 6XQO) monomer structures. **b** Structural comparison of the N-lobe between *Dd*MICU and *Hs*MICU1. The two structures are aligned based on the C-lobe, which is represented as a space-filling model. The tilt angle of the N-lobe is marked with a black arrow. **c** Superimposition of the N-lobe structures of *Dd*MICU and *Hs*MICU1. **d** Close-up view of the interaction residues involved in the EFb motif. **e** Superimposition of the C-lobe structures of *Dd*MICU and *Hs*MICU1. The N-lobe, bridge helix and C-lobe of *Dd*MICU are colored cyan, green and pink; *Hs*MICU1 is colored gray. The Ca^{2+} bound in *Dd*MICU and *Hs*MICU1 is shown as red and gray spheres, respectively.

Dimer formation and oligomeric states of *Dd*MICU

Both the F-F and B-B dimers are crucial for gatekeeping in the human MCU complex, and an O-shaped holo-complex is formed in the high Ca^{2+} state through the B-B dimer interaction in *Hs*MICU2[30–32]. Although the B-B dimer was not observed in the *Dd*MICU crystal, we identified a unique dimeric state, the "Head-to-Head (H-H)" dimer (Fig. 5a). The H-H dimer of *Dd*MICU was observed in an asymmetric unit and was able to form a tetrameric structure through interaction with the F-F dimer (Fig. 5c). To analyze the oligomeric states of *Dd*MICU in solution, we performed multi-angle light scattering coupled with size exclusion

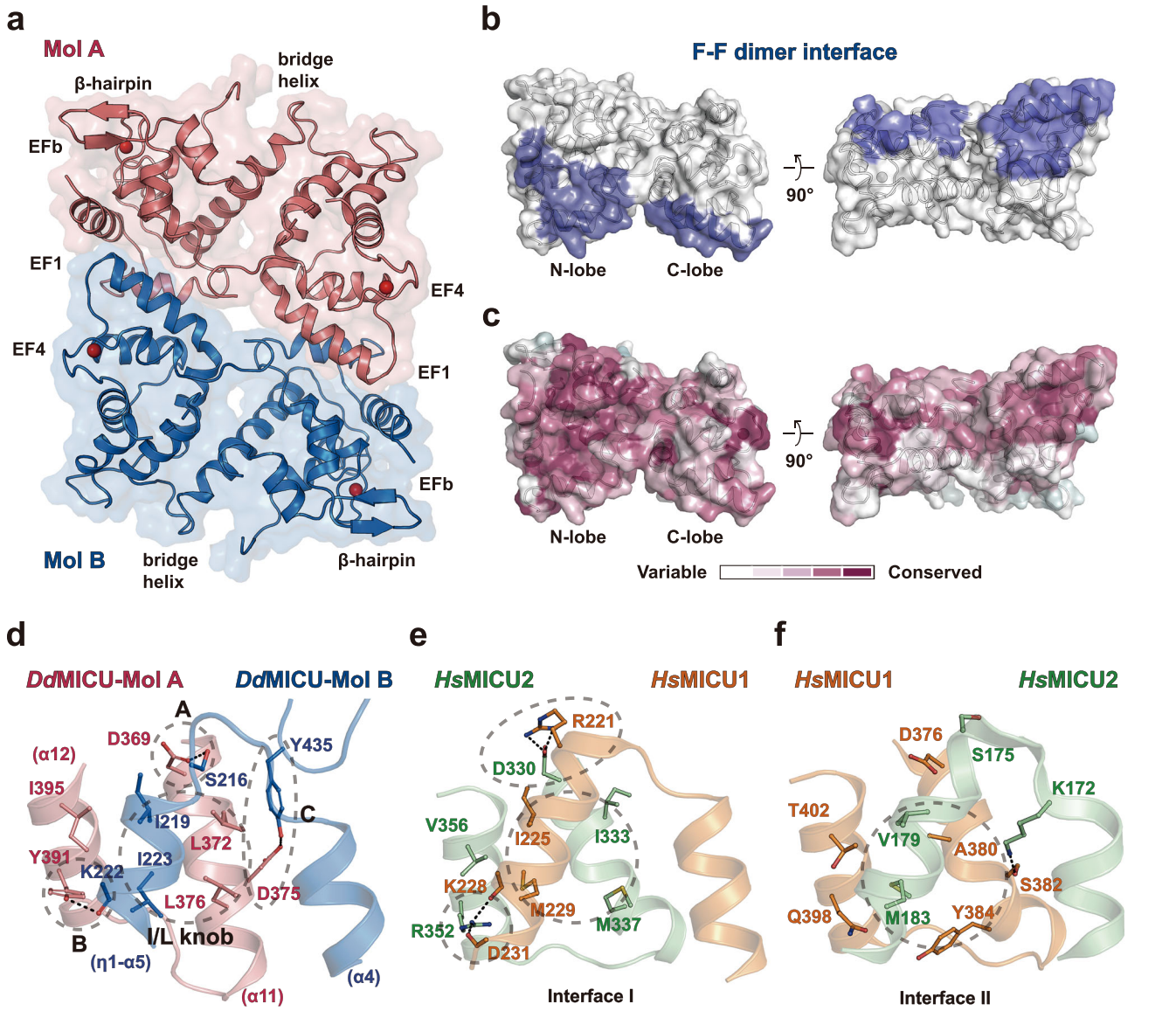

Fig. 4 | F-F dimer of *Dd*MICU and comparison with *Hs*MICU1. a Cartoon and space-filling representations of the F-F dimer of *Dd*MICU. **b** Representations of the F-F dimer interface in *Dd*MICU using space-filling models. The F-F dimer interface is colored slate. **c** Sequence conservation of *Dd*MICU depicted with a space-filling model. Conserved sequences are colored from white (variable, grade 5) to burgundy (conserved, grade 9) according to ConSurf color coding. **d**–**f** Interactions at the *Dd*MICU F-F dimer interface (**d**), *Hs*MICU1-*Hs*MICU2 (PDB code: 6XQO) interface I (**e**) and *Hs*MICU1-*Hs*MICU2 interface II (**f**). Mol A and Mol B of *Dd*MICU are colored red and blue, respectively; *Hs*MICU1 and *Hs*MICU2 are colored orange and green.

chromatography (SEC-MALS). The calculated molar mass (M_w) of the *Dd*MICU in solution was 169.9 ± 2.2, 114.4 ± 7.9, 97.5 ± 9.5 and 92.4 ± 1.2 kDa at [NaCl] = 50, 100, 150 and 300 mM, respectively (Fig. 5d). These results suggest *Dd*MICU is a tetramer at the low ionic strength of 50 mM, but as the ionic strength increases the equilibrium of the oligomeric state shifts to the dimer at ionic strengths of 150 mM or higher.

We also analyzed the interface residues of the H-H dimer of *Dd*MICU in detail. The interface of the *Dd*MICU H-H dimer included several hydrogen bonds (Fig. 5b). The mainchain carbonyl group of Gly228 and Asp229, located at the loop of the EF1 motif in Mol B, formed hydrogen bonds with Lys394 and Asp400 in Mol A. Asp229 participated in both the interface interaction of the H-H dimer and the Ca^{2+} coordination in the EF1 motif. Arg280 and Gln285 of Mol B participated in hydrogen bond networks with Arg295 and Asp355 of Mol A, which were mediated by one water molecule. To confirm whether the H-H dimer interface interactions contribute to tetramerization, we purified an H-H dimer mutant (*Dd*MICU^{4Ala}; Q285A/R295A/D355A/K394A) and conducted SEC-MALS assays in [NaCl] = 50 and 300 mM (Supplementary Fig. 6). The calculated M_w of the *Dd*MICU^{4Ala} in solution was 88.4 ± 1.5 and 83.7 ± 0.3 kDa at [NaCl] = 50 and 300 mM, respectively, indicating that the H-H dimer interface interaction is critical for tetramerization. To further assess the structural contribution of the H-H dimer interface, we analyzed its interface area, which was approximately 650 Å^2, similar to that of B-B dimers (~700 Å^2) but narrower than that of F-F dimers (~1200 Å^2) in human MICUs (Table 3). The calculated binding energy of the *Dd*MICU H-H dimer was −8.7 kcal/mol, which was similar to that of the F-F dimers (−8.4 kcal/mol) in human MICUs but lower than that of the B-B dimers of *Hs*MICU2 and *Hs*MICU3 (−7.5 kcal/mol). Thus, the H-H dimer interface in *Dd*MICU includes several hydrogen bonds and may form an energetically stable dimer similar to the F-F dimers in human MICUs. This suggests the H-H dimer interaction could contribute to the oligomeric assembly of *Dd*MICU, potentially influencing its regulatory function in the *Dd*MCU complex.

Table 3 | Dimer interface analysis of MICU structures

Dimer formation		H-H dimer	F-F dimer					B-B dimer	
Protein (PDB code)		*Dd*MICU (9K6M)	*Dd*MICU (9K6M)	*Hs*MICU1 (4NSD)	*Hs*MICU1-2 (6XQO)	*Hs*MICU2 (6IIH)	*Hs*MICU3 (6AGI)	*Hs*MICU2 (6IIH)	*Hs*MICU3 (6AGI)
Interface area (Å^2)		650	1370	470	1310	1260	1640	760	640
Number of interfacial contacts (ICs)	charged-charged	16	2	6	4	8	8	9	6
	charged-polar	15	6	4	9	7	9	8	6
	charged-apolar	11	20	9	15	15	26	23	10
	polar-polar	2	0	1	4	3	4	2	4
	polar-apolar	8	16	4	17	7	10	2	7
	apolar-apolar	2	48	4	32	39	54	13	12
ΔG (kcal/mol)		−8.7	−10.6	−6.6	−9.6	−8.2	−9.3	−8.0	−6.9
K_d (M)		4.2×10^{-7}	1.7×10^{-8}	1.4×10^{-7}	9.7×10^{-8}	9.8×10^{-7}	1.5×10^{-7}	1.4×10^{-6}	9.3×10^{-6}

Liposome binding properties of *Dd*MICU through the C-terminal helix

The C-terminal helix (C-helix) of *Hs*MICU1 is crucial for its gatekeeping function and directly interacts with the membrane and *Hs*MCU[30,46]. Because the C-helix of *Dd*MICU (444-TGIFSKFKKILKVLT-458) was poorly defined in the electron density maps due to the flexibility of the crystal lattice, we modeled the C-helix of *Dd*MICU and analyzed its characteristics (Fig. 6a). We found that the C-helix of *Dd*MICU is amphipathic, consisting of positively charged and hydrophobic residues on opposite sides (Fig. 6b). Four lysine residues gathered on one side to form a positively charged face, while seven hydrophobic residues gathered to form the opposite hydrophobic face. Comparison of the properties of the C-helices in *Dd*MICU and *Hs*MICU1 using the HELIQUEST[47] server revealed that the mean hydrophobicity (H) of the C-helix of *Dd*MICU is similar to that of *Hs*MICU1 (0.58). In *Dd*MICU, however, the net charge (z) was twice as high (*Dd*MICU: 4, *Hs*MICU1: 2), and the hydrophobic moment (μH) was stronger (*Dd*MICU: 0.68, *Hs*MICU1: 0.55) (Supplementary Fig. 7). These observations raise the possibility that the C-helix of *Dd*MICU may also participate in membrane binding. We then performed liposome flotation assays using wild-type *Dd*MICU and a C-helix deletion construct (*Dd*MICU$^{\Delta C}$) to investigate whether *Dd*MICU would interact with liposomes serving as a peripheral membrane model (Fig. 6c, Supplementary Figs. 8 and 9). *Dd*MICU bound to liposomes under both Ca^{2+} and EGTA conditions. This is consistent with earlier findings for *Hs*MICU1, which also bound to liposomes, irrespective of the presence of Ca^{2+} or EGTA[22,31]. However, unlike *Hs*MICU1, which bound to liposomes with or without its C-helix, *Dd*MICU$^{\Delta C}$ did not bind to liposomes, despite the presence of cardiolipin. This suggests the C-helix of *Dd*MICU plays a key role in membrane binding in a MCU system lacking an EMRE.

Discussion

The MCU complex plays a key role in regulating mitochondrial Ca^{2+} homeostasis, which is essential for cellular function as well as mitochondrial metabolism, and is tightly regulated by essential regulatory proteins such as MICUs and the EMRE. Unlike in metazoans, the non-metazoan MCU complex is characterized by the MCU's ability to take up Ca^{2+} without the EMRE[38]. This means that the Ca^{2+} uptake function of the MCU is directly regulated by a MICU. Despite the importance of non-metazoan MICUs being able to control MCU complexes without an EMRE, the molecular structure and underlying mechanism of non-metazoan MICUs were lacking. We therefore determined the crystal structure of *Dd*MICU to study the non-metazoan MICU in an EMRE-free MCU complex system.

The overall structure of *Dd*MICU is similar to that of human MICUs in that it is composed of an N-lobe, bridge helix, and C-lobe (Figs. 1b and 3a). *Dd*MICU contains three canonical EF-hand motifs: the EF1 and EF4 motifs as well as a non-metazoan-specific EFb motif (Fig. 2a). These three motifs have conserved canonical EF-hand sequences with pentagonal bipyramidal geometry and a structure that is stabilized by Ca^{2+} binding (Supplementary Fig. 3). Moreover, the K_d values for Ca^{2+} binding to all three EF-hand motifs in *Dd*MICU are approximately 0.3 μM, which is comparable to the K_d values of *Hs*MICU1 (Fig. 2b). The Ca^{2+} uptake threshold of the human MCU regulated by MICUs is comparable to the K_d value of the EF-hand motifs in each MICU[22]. It is therefore likely that the Ca^{2+} uptake threshold of the *Dd*MCU regulated by *Dd*MICU is comparable to the K_d values of its EF-hand motifs. The *Dd*MICU F-F dimer also showed structural similarity to the *Hs*MICU1-*Hs*MICU2 dimer (Fig. 4a and Supplementary Fig. 4), with conserved hydrophobic and electrostatic interactions at the dimer interface (Fig. 4b, c). Given the structural resemblance between *Dd*MICU and human MICUs and conservation of key interface interactions, it is likely that the structural changes elicited by Ca^{2+} binding to the EF1 and EF4 motifs located at the dimer interface of *Dd*MICU are similar to those observed in the *Hs*MICU1-*Hs*MICU2 dimer. Consequently, the Ca^{2+} uptake function of the *Dd*MCU may be regulated by structural changes to *Dd*MICU at the Ca^{2+} uptake threshold, which are likely comparable to those in *Hs*MICU1.

Cryo-EM structures of the human MCU holo-complex revealed that the gating mechanism of the human MCU complex is dependent on interactions between MICU1-MICU2 and MCU-EMRE[30–32,48]. MICU1 acts as a gatekeeper for the MCU, blocking the IMS entrance at resting [Ca^{2+}] levels and controlling its opening through Ca^{2+}-dependent interactions with the MCU pore[17,33–35]. Notably, under high Ca^{2+} conditions, an O-shaped MCU holo-complex is formed through interactions between MICU1 and EMRE involving electrostatic interactions between the poly K domain of MICU1 and the poly D domain of EMRE, with no direct MCU-MICU interactions[30–32]. Furthermore, a working model of the human MCU complex suggests the apo *Hs*MICU1-*Hs*MICU2 heterodimer detaches from the *Hs*MCU pore due to steric hindrance with the membrane as Ca^{2+} levels rise[31]. Similarly, if we aligned the model of the F-F dimer of the Ca^{2+}-bound *Dd*MICU structure with the apo state model with the same MCU pore interactions, *Dd*MICU would also be expected to clash with the membrane surface and be dislodged from the *Dd*MCU pore in the Ca^{2+}-bound state (Supplementary Fig. 10). This suggests the mechanism by which the *Dd*MICU regulates Ca^{2+} uptake shares similarities with that of *Hs*MICUs, despite the lack of an EMRE. We therefore speculate that at low Ca^{2+} concentrations (less than 0.3 μM), *Dd*MICU binds to the *Dd*MCU through conserved MCU interaction motifs, blocking the *Dd*MCU pore and acting as a gatekeeper. At higher Ca^{2+} concentrations (0.3 μM or above), Ca^{2+} binding to the EF-hand motifs of *Dd*MICU induces a structural change that causes *Dd*MICU to dissociate from the *Dd*MCU (Fig. 7a). Despite detaching from the *Dd*MCU pore, we suggest the amphipathic C-helix of *Dd*MICU interacts with the membrane, preventing *Dd*MICU from detaching from the mitochondrial inner-membrane and keeping it in close proximity to the *Dd*MCU.

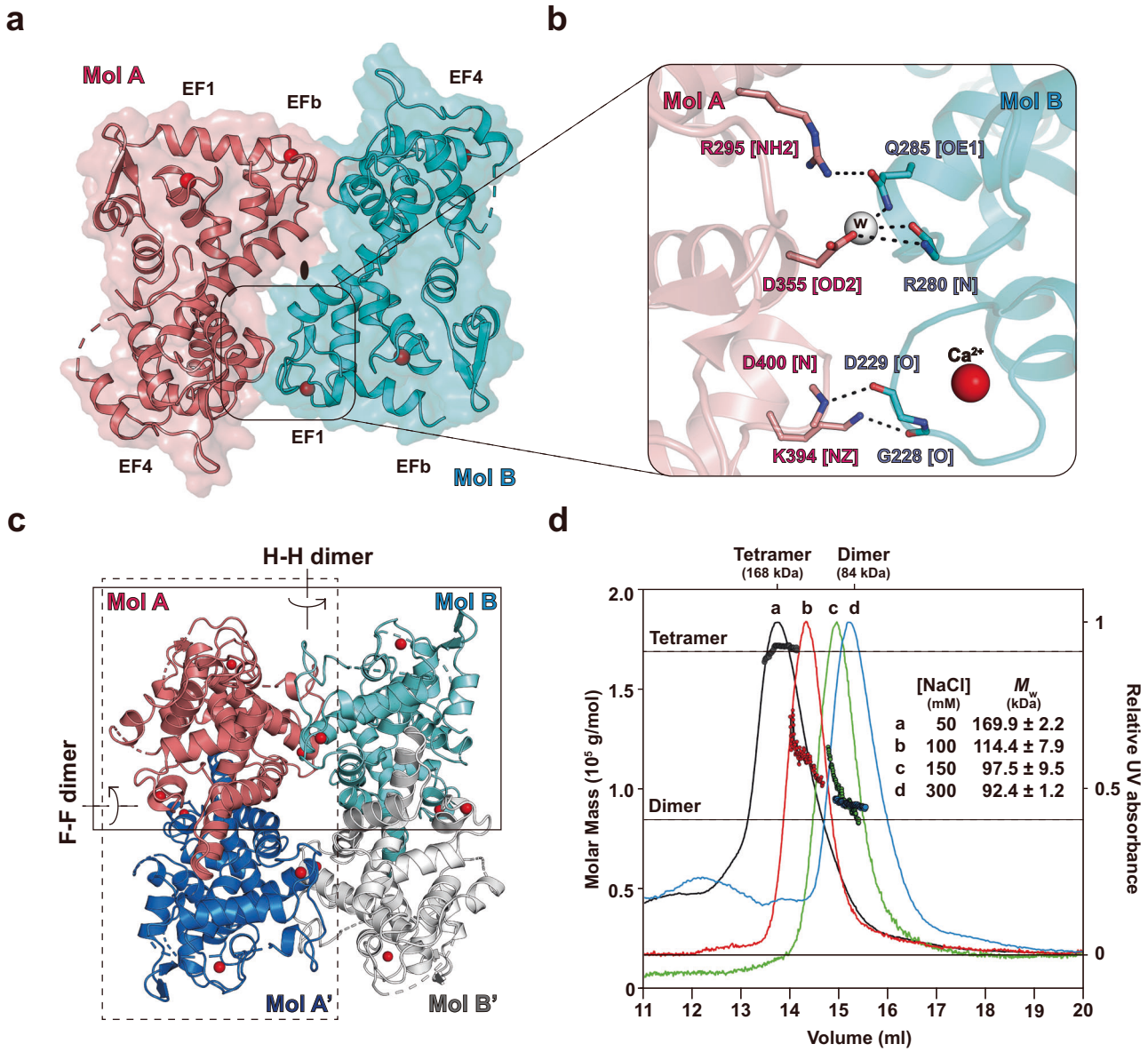

Fig. 5 | Structural and biochemical analysis of the *Dd*MICU H-H dimer and tetramer. a Cartoon and space-filling representations of the H-H dimer of *Dd*MICU. **b** Close-up view of the H-H dimer interface interactions. The interaction residues are shown as sticks, with interactions depicted as dotted lines. Ca^{2+} is shown as a red sphere, a water molecule (w) as a white sphere. **c** Structure of the *Dd*MICU tetramer. Mol-A, Mol-B, Mol-A' and Mol-B' of *Dd*MICU are colored red, cyan, blue and gray, respectively. Ca^{2+} is shown as red spheres. The asymmetric unit of the *Dd*MICU crystal is outlined with gray lines (H-H dimer), and the crystallographic two-fold symmetry is indicated by a gray-dotted line (F-F dimer). **d** SEC-MALS assay of *Dd*MICU in solution with NaCl concentrations of 50 mM (black), 100 mM (red), 150 mM (green) and 300 mM (blue). The relative UV absorbance at 280 nm is shown as a line, with calculated molar masses represented by circles and indicated as the mean ± standard deviation.

We observed that *Dd*MICU forms a H-H dimer, which further assembles into a tetramer through interactions with the F-F dimer interface (Fig. 5b, Supplementary Fig. 6). The tetramerization of the *Dd*MICU was dependent on solution ionic strength, and *Dd*MICU was present in an equilibrium between tetrameric and dimeric forms at physiological ionic strength (i.e., 100–150 mM) (Fig. 5d). The tetramer, including the H-H dimer, represents a distinct oligomeric structure that has not been observed with human MICUs. With *Dd*MICU in the tetrameric state, its MCU interaction residues in the N-terminus and C-terminus helices are oriented in opposite directions. Consequently, the *Dd*MCU holo-complex is likely to be oriented horizontally (Fig. 7b). Given that the *Hs*MICU1 homo-hexamer is crucial for maintaining the cristae junction[49], the *Dd*MCU holo-complex may also be positioned at the cristae junction and contribute to its maintenance. Further studies will be necessary to ascertain whether *Dd*MICU is involved in cristae junction formation and plays a key role in cristae separation via its multimeric states.

In summary, we report the structural characteristics of *Dd*MICU in the Ca^{2+}-bound state, highlighting its three canonical EF-hand motifs, which bind Ca^{2+}, and its oligomeric states. We suggest *Dd*MICU acts as a gatekeeper for the *Dd*MCU, blocking the pore at Ca^{2+} concentrations below 0.3 μM and dissociating upon Ca^{2+} binding. The membrane-anchoring C-helix of the *Dd*MICU may help to stabilize its proximity to the *Dd*MCU. These structural insights suggest a Ca^{2+}-dependent regulatory mechanism similar to that of metazoan MICUs, with additional regulatory features influenced by the C-helix of MICUs and its unique tetrameric structure. Given these findings, further studies will be needed to investigate the structural and functional features underlying the mechanism governing this MCU complex system, which lacks an EMRE.

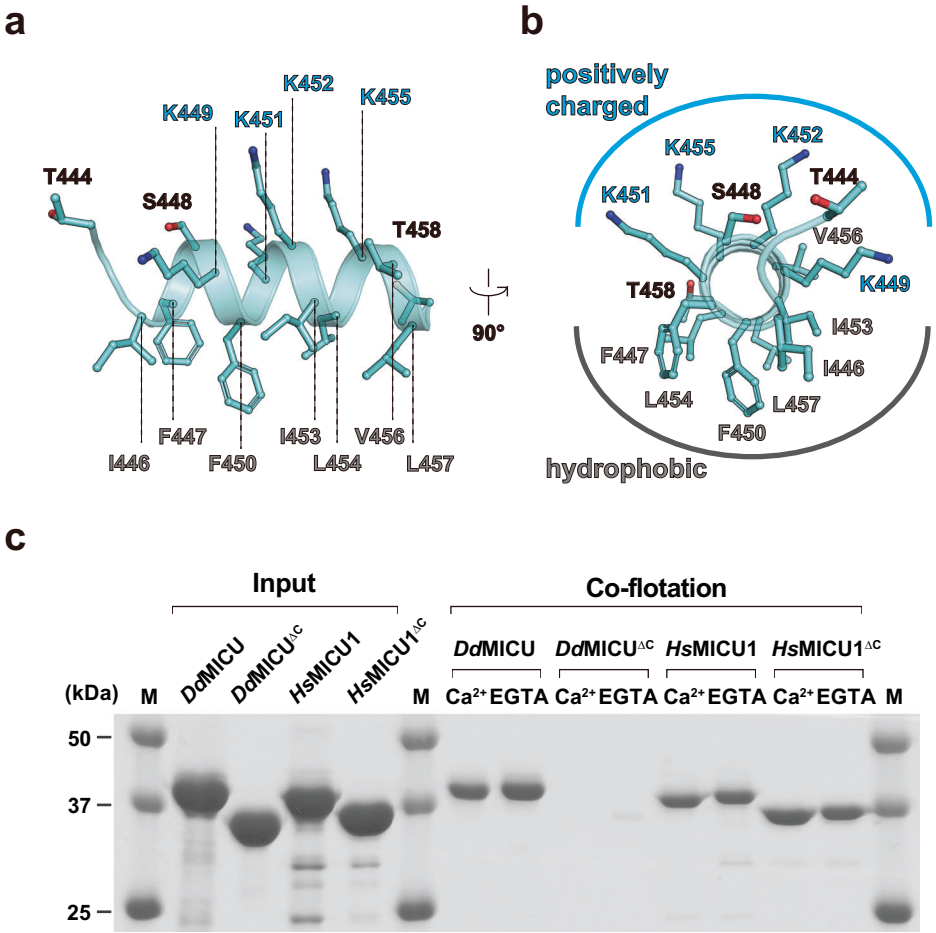

Fig. 6 | Biochemical and structural characteristics of the C-helix in *Dd*MICU. a Side view cartoon representation of the C-helix in *Dd*MICU. Side chains are depicted as ball-and-stick models. Positively charged, hydrophobic and polar residues are labeled in blue, gray and black, respectively. **b** Front view cartoon representation of the C-helix in *Dd*MICU. **c** Liposome flotation assay with *Dd*MICU, *Dd*MICU$^{\Delta C}$, *Hs*MICU1, and *Hs*MICU1$^{\Delta C}$. Proteins were resolved by 12% SAS-PAGE gel, with the size marker (M) indicated.

Materials and methods

Cloning and purification of the *Dd*MICU constructs

*Dd*MICU (EAL63559.1, residues 105–461) was optimized with the *Escherichia coli* (*E. coli*) codon and synthesized (GenScript). *Dd*MICU wild-type, EF-hand single mutants (*Dd*MICU$^{\Delta EFb}$; E202A, *Dd*MICU$^{\Delta EF1}$; E236A, *Dd*MICU$^{\Delta EF4}$; E425A), EF-hand double mutants (*Dd*MICU^{EFb}; E236A/E425A, *Dd*MICU^{EF1}; E202A/E425, *Dd*MICU^{EF4}; E202A/E236A), *Dd*MICU$^{\Delta C}$ (residues 105-437), and *Dd*MICU^{4Ala} (Q285A/R295A/D355A/K394A) constructs were amplified and cloned into a modified pRSFDuet-1 (Novagen) expression vector that had a hexahistidine (6×His) tag at its N-terminus. The recombinant vectors were transformed into *E. coli* BL21 (DE3) and grown in Luria-Bertani (LB) medium containing 50 μg/mL kanamycin at 37 °C until the UV absorbance at 600 nm was 0.6. Overexpression of the recombinant protein was induced by addition of 0.2 mM isopropyl β-D-1-thiogalactopyranoside (IPTG) at 20 °C for 18 h.

Cells were harvested by centrifugation (4000 × *g*) for 20 min at 4 °C, resuspended in buffer A [50 mM Tris-HCl pH 8.5, 500 mM NaCl, 5 mM imidazole, 5 mM $CaCl_2$, 5 mM β-mercaptoethanol, and 5% (*v*/*v*) glycerol] and lysed by sonication. After centrifugation (15,000 × *g*) of the lysates for 1 h, the supernatants were loaded onto an Econo-Column (Bio-Rad) packed with Ni-IDA agarose resin (Elpis-Biotech) pre-equilibrated with buffer A. The bound protein was washed with buffer B [20 mM Tris-HCl pH 8.5, 500 mM NaCl, 40 mM imidazole, 5 mM $CaCl_2$, 5 mM β-mercaptoethanol, and 5% (*v*/*v*) glycerol] and eluted with buffer C (20 mM Tris-HCl pH 8.5, 500 mM NaCl, 300 mM imidazole, 5 mM $CaCl_2$, and 5 mM β-mercaptoethanol). The eluate was concentrated to 5 mL using an Amicon Ultra-15 30 K (Millipore, Merck) and further purified through size exclusion chromatography (SEC) on a HiLoad 16/60 Superdex 200 prep (Pharmacia) column pre-equilibrated with SEC buffer A (20 mM MES-NaOH pH 6.8, 100 mM NaCl, 5 mM $CaCl_2$, and 5 mM DL-dithiothreitol). The single peak fractions were collected, concentrated up to 10 mg/mL, and stored at -80°C.

For seleno-L-methionine (Se-Met) incorporation, methionine-auxotrophic *E. coli* B834 (DE3) (Novagen) cells were transfected with a recombinant vector, pre-cultured in LB medium and harvested by centrifugation (4000 × *g*) for 20 min at 4 °C. The pellet was resuspended in M9 minimal medium [M9 medium supplemented with 50 μg/mL Se-Met, 0.4% (*w*/*v*) glucose, 0.004% (*w*/*v*) thiamine, 2 mM $MgSO_4$, 0.2 mM $CaCl_2$ and amino acids] to wash out the LB medium and harvested again by centrifugation. After the washing step, a resuspension of the cell pellet in M9 minimal medium was transferred to a fresh culture in 2 L of M9 minimal medium. The overall procedure to purify the Se-Met derivative of *Dd*MICU was the same as for native *Dd*MICU.

Crystallization of the *Dd*MICU

To crystallize native and Se-Met *Dd*MICU, initial screening was performed using the sitting-drop vapor diffusion method in a 96-well INTELLI-PLATE (Art Robbins Ins.) by mixing 0.2 μL of the protein and 0.2 μL of reservoir solution. After one to two weeks, native and Se-Met *Dd*MICU formed microcrystals in reservoir solution containing PACT Premier (Molecular Dimensions) and Wizard Classic 3 & 4 (Rigaku Reagents). Additional crystallization trials were performed using the hanging-drop vapor-diffusion method in a 24-well VDX plate (Hampton Research) by mixing 2 μL of the protein and 1 μL of the reservoir solution. Final optimized native and Se-Met *Dd*MICU crystals were obtained in a reservoir solution containing [0.1 M MIB buffer (Molecular Dimensions) pH 5.5, 20% (*w*/*v*) PEG 1500, 10 mM 3-((3-cholamidopropyl) dimethylammonio)-1-propanesulfonate (CHAPS), and 10 mM tris(2-carboxyethyl)phosphine (TCEP)] and [0.1 M MMT buffer (Molecular Dimensions) pH 7.0, 25% (*w*/*v*) PEG 1500, 0.1 M guanidine hydrochloride, 16 mM CHAPS and 10 mM TCEP],

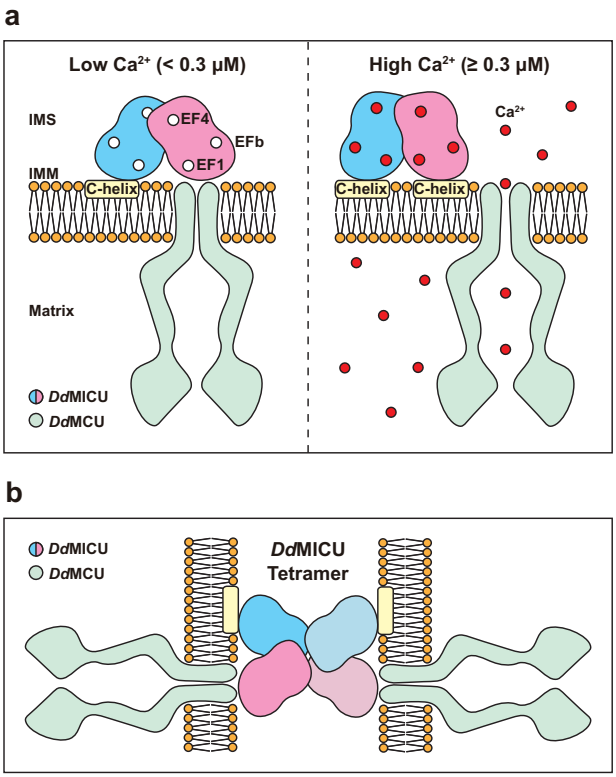

Fig. 7 | Proposed model for Ca^{2+} uptake via the *Dd*MCU-*Dd*MICU complex. **a** Model of the *Dd*MCU-*Dd*MICU complex in low and high Ca^{2+} states. In the resting condition, *Dd*MICU binds to the *Dd*MCU pore and the membrane through conserved N-terminal residues and the C-helix. In the high Ca^{2+} state, *Dd*MICU dissociates from the *Dd*MCU, enabling Ca^{2+} uptake through the *Dd*MCU. *Dd*MICU remains anchored to the membrane via its C-helix. **b** Horizontal model of the *Dd*MCU-*Dd*MICU holo-complex. IMS, IMM, and Matrix indicate the intermembrane space, inner mitochondrial membrane, and mitochondrial matrix, respectively.

respectively. Crystals were cryoprotected by soaking for 10 min in mother liquor containing an additional 20% (*v*/*v*) ethylene glycol before flash freezing in liquid nitrogen.

Data collection, structure determination, and analysis

Native and SAD data sets were collected at a wavelength of 0.9794 Å on beamlines 5C and 7A at the Pohang Accelerator Laboratory (PAL) (Pohang, Korea). We collected the best resolution diffraction data for native *Dd*MICU at 2.5 Å resolution and for Se-Met *Dd*MICU at 3.5 Å resolution. Data indexing, integration and scaling were performed using the XDS package[50] and HKL suite[51]. Both native and Se-Met *Dd*MICU crystals were in the tetragonal space group $I4_122$ ($a = b = 103.9$ Å and $c = 297.5$ Å for native *Dd*MICU, $a = b = 104.5$ Å and $c = 295.0$ Å for Se-Met *Dd*MICU). Because we were not able to solve the structure using the molecular replacement (MR) method with the human MICU structure, we used MR-SAD methods to solve the *Dd*MICU structure. The 3.5 Å resolution data from Se-Met *Dd*MICU were used to obtain the initial phase information and model from the anomalous dispersion of selenium with AutoSol and AutoBuild in the PHENIX package[52]. Using this initial model, we performed additional phase refinement and model building with Phaser-MR and Phaser-EP in the PHENIX package and with Coot[53] using native *Dd*MICU data. The final model was refined and modeled after iterative cycles with phenix.refine in the PHENIX package, REFMAC5 in the CCP4i suite[54], and Coot. The coordinates and structural factors were deposited in the PDB RCSB with an accession code of 9K6M. PyMOL[55] version 2.5.0 was used for all structural figures, and PDBePISA[56] and PRODIGY[57] were used for interface analysis. The C-helix of *Dd*MICU and the apo state of the *Dd*MCU-*Dd*MICU complex were modeled using AlphaFold 3[58]. The characteristics of the C-helix was analyzed with HELIQUEST[47].

Sequence alignment and domain composition analysis

Multiple sequence alignments were performed using the Muscle algorithm in MEGA-X[59] and graphically displayed using ESPript 3.0[60]. Domain compositions of MICU proteins were identified with the PROSITE[61] database using a list of 650 MICU sequences analyzed by Pittis et al.[37]. Sequence conservation of *Dd*MICU was visualized using the ConSurf[62] server.

Microscale thermophoresis analysis

The Ca^{2+} binding affinities of *Dd*MICU EF-hand mutants were measured using MST assays. For those assays, purified *Dd*MICU EF-hand double mutants were subjected to further gel filtration in SEC buffer B (20 mM HEPES-NaOH pH 7.0, 300 mM NaCl, 5 mM EGTA, and 5 mM DL-dithiothreitol) using a Superdex 200 10/300 GL column (GE Healthcare). To remove the remaining Ca^{2+} and EGTA, we dialyzed with SEC buffer B without EGTA for 48 h at 4 °C. The residual Ca^{2+} was measured after dialysis using the Ca^{2+}-indicator fura-2 [non-acetoxymethyl ester (AM) form, Molecular Probes, Eugene, OR], which confirmed that the remaining Ca^{2+} concentration was less than 10 nM. The 6×His proteins (500 nM) were labeled using a His-Tag Labeling Kit-RED-tris-NTA 2nd Generation (NanoTemper Technologies) and incubated with serially diluted $CaCl_2$ (12 pM-400 μM). To minimize surface adsorption and improve the homogeneity of the sample, we added 0.05% (*v*/*v*) Tween-20 and 0.1% (*w*/*v*) BSA to the buffer used to dilute all components. After combining the various components, the samples were incubated at room temperature for 30 min prior to being loaded into standard capillaries (NanoTemper Technologies). The MST assays were performed in triplicate ($n = 3$) using a Monolith NT.115 Pico instrument (NanoTemper Technologies, Germany), and the data were analyzed using MO.Affinity Analysis version 2.3 (NanoTemper Technologies)[63,64].

Heat aggregation assay

The melting temperatures of *Dd*MICU wild-type and its EF-hand mutants were determined spectrophotometrically as described previously[65]. Briefly, 100 μM purified protein in SEC buffer A was placed in PCR tubes, and the temperature was increased at the rate of 4 °C per 90 s using a Thermal Cycler Dice Gradient (Takara Bio, Inc.). Turbidity was measured based on the absorption at 470 nm using a Nanodrop-2000 spectrophotometer (Thermo Fisher Scientific, Inc.). The dose-response curve was fitted using OriginLab Pro 9.1, and the melting temperature (T_m) was labeled at the bottom right. All experiments were done in triplicate ($n = 3$). Data are presented as the mean ± 95% confidence interval (CI) based on the two-tailed t-distribution.

SEC-MALS of *Dd*MICU

To characterize the oligomeric state of the *Dd*MICU, size-exclusion chromatography coupled to multi-angle light scattering (SEC-MALS) was performed using a Superdex 200 10/300 GL column (GE Healthcare) connected to a MALS detector (MiniDAWN TREOS, Wyatt Technology) and a differential refractometer (Optilab rEX, Wyatt Technology). Aliquots of purified *Dd*MICU in a volume of 200 μl at 2.0 mg/mLwere loaded into the column pre-equilibrated with SEC buffer A containing different NaCl concentrations normalized using bovine serum albumin. Weight-average molar masses were analyzed using the Zimm model for fitting and calculated using ASTRA 6 software (Wyatt Technology). The solvent refractive index and viscosity values were defined as 1.33 and 0.89 cP. The dn/dc value for all samples was 0.185 mL/g, a standard value for proteins.

Liposome preparation and flotation assays

A mixture of phosphatidylethanolamine (PE), phosphatidylcholine (PC) and cardiolipin (CL) (Avanti Polar Lipids, Inc.) at a ratio of 5:3:2 (*w*/*w*) was dissolved in chloroform and dried using an IKA RV 8 rotary evaporator (IKA, Inc.). The dried lipids were then hydrated in SEC buffer C (20 mM HEPES-NaOH pH 7.0, 300 mM NaCl, and 5 mM DL-dithiothreitol) to a

final concentration of 10 mg/mL. All buffers contained either 5 mM $CaCl_2$ or EGTA, depending on the experimental conditions. Following vortexing, liposomes were formed by freeze-thawing five times and extrusion ten times through a 200 nm filter using an Avanti Mini-extruder (Avanti Polar Lipids, Inc.) at 65 °C.

For the protein flotation assay, 500 µg of protein-free liposomes were mixed with 50 µg of protein in SEC buffer C to a final volume of 350 µl. The mixture was incubated for 10 min at room temperature, then mixed 1:1 with an 80% (*w*/*v*) HistoDenz™ (Sigma-Aldrich, Merck) solution in SEC buffer C. That mixture was added to the bottom layer of an open-top thick-walled polycarbonate tube (Beckman). A 600 µl layer of 30% HistoDenz™ solution in SEC buffer C was then added on top, followed by a 200 µl layer of SEC buffer C. The gradient was centrifuged at 259,000 × *g* for 3 h at 4 °C using an Optima MAX-TL ultracentrifuge with a TLS-55 rotor (Beckman). Liposomes were collected from the top layer, sampled and subjected to SDS-PAGE, followed by Coomassie staining. *Hs*MICU1 (97–476) and *Hs*MICU1$^{\Delta C}$ (97–444) were used as positive controls. These proteins were purified using the same method described previously[29].

Statistics and reproducibility

Error bars represent the mean ± standard deviation (SD) or mean ± 95% confidence interval (CI), based on at least three biologically independent experiments. The 95% CI was calculated based on the two-tailed *t*-distribution.

Reporting summary

Further information on research design is available in the Nature Portfolio Reporting Summary linked to this article.

Data availability

The coordinates and structural factors of the *Dd*MICU have been deposited in the Protein Data Bank (PDB code: 9K6M). The source data underlying the graphs presented in the paper are provided in Supplementary Data 1. All other data are available from the corresponding author upon reasonable request.

Received: 29 October 2024; Accepted: 13 May 2025;
Published online: 21 May 2025

References

1. Clapham, D. E. Calcium signaling. *Cell* **131**, 1047–1058 (2007).
2. Rizzuto, R., De Stefani, D., Raffaello, A. & Mammucari, C. Mitochondria as sensors and regulators of calcium signalling. *Nat. Rev. Mol. Cell Biol.* **13**, 566–578 (2012).
3. Kamer, K. J. & Mootha, V. K. The molecular era of the mitochondrial calcium uniporter. *Nat. Rev. Mol. Cell Biol.* **16**, 545–553 (2015).
4. Giorgi, C., Marchi, S. & Pinton, P. The machineries, regulation and cellular functions of mitochondrial calcium. *Nat. Rev. Mol. Cell Biol.* **19**, 713–730 (2018).
5. Marchi, S., Giorgi, C., Galluzzi, L. & Pinton, P. Ca^{2+} fluxes and cancer. *Mol. Cell* **78**, 1055–1069 (2020).
6. Finkel, T. et al. The ins and outs of mitochondrial calcium. *Circ. Res.* **116**, 1810–1819 (2015).
7. Raffaello, A., Mammucari, C., Gherardi, G. & Rizzuto, R. Calcium at the center of cell signaling: interplay between endoplasmic reticulum, mitochondria, and lysosomes. *Trends Biochem. Sci.* **41**, 1035–1049 (2016).
8. Kirichok, Y., Krapivinsky, G. & Clapham, D. E. The mitochondrial calcium uniporter is a highly selective ion channel. *Nature* **427**, 360–364 (2004).
9. Baughman, J. M. et al. Integrative genomics identifies MCU as an essential component of the mitochondrial calcium uniporter. *Nature* **476**, 341–345 (2011).
10. De Stefani, D., Raffaello, A., Teardo, E., Szabo, I. & Rizzuto, R. A forty-kilodalton protein of the inner membrane is the mitochondrial calcium uniporter. *Nature* **476**, 336–340 (2011).
11. Raffaello, A. et al. The mitochondrial calcium uniporter is a multimer that can include a dominant-negative pore-forming subunit. *EMBO J.* **32**, 2362–2376 (2013).
12. Sancak, Y. et al. EMRE is an essential component of the mitochondrial calcium uniporter complex. *Science* **342**, 1379–1382 (2013).
13. Mallilankaraman, K. et al. MCUR1 is an essential component of mitochondrial Ca^{2+} uptake that regulates cellular metabolism. *Nat. Cell Biol.* **14**, 1336–1343 (2012).
14. Perocchi, F. et al. MICU1 encodes a mitochondrial EF hand protein required for Ca^{2+} uptake. *Nature* **467**, 291–296 (2010).
15. Plovanich, M. et al. MICU2, a paralog of MICU1, resides within the mitochondrial uniporter complex to regulate calcium handling. *PLoS One* **8**, e55785 (2013).
16. Vecellio Reane, D. et al. A MICU1 splice variant confers high sensitivity to the mitochondrial Ca^{2+} uptake machinery of skeletal muscle. *Mol. Cell* **64**, 760–773 (2016).
17. Tsai, C.-W. et al. Mechanisms and significance of tissue-specific MICU regulation of the mitochondrial calcium uniporter complex. *Mol. Cell* **82**, 3661–3676.e3668 (2022).
18. Csordas, G. et al. MICU1 controls both the threshold and cooperative activation of the mitochondrial Ca^{2+} uniporter. *Cell Metab.* **17**, 976–987 (2013).
19. Mallilankaraman, K. et al. MICU1 is an essential gatekeeper for MCU-mediated mitochondrial Ca^{2+} uptake that regulates cell survival. *Cell* **151**, 630–644 (2012).
20. Wang, L. et al. Structural and mechanistic insights into MICU1 regulation of mitochondrial calcium uptake. *EMBO J.* **33**, 594–604 (2014).
21. Petrungaro, C. et al. The Ca^{2+}-dependent release of the Mia40-induced MICU1-MICU2 dimer from MCU regulates mitochondrial Ca^{2+} Uptake. *Cell Metab.* **22**, 721–733 (2015).
22. Kamer, K. J., Grabarek, Z. & Mootha, V. K. High-affinity cooperative Ca^{2+} binding by MICU1-MICU2 serves as an on-off switch for the uniporter. *EMBO Rep.* **18**, 1397–1411 (2017).
23. Patron, M., Granatiero, V., Espino, J., Rizzuto, R. & De Stefani, D. MICU3 is a tissue-specific enhancer of mitochondrial calcium uptake. *Cell Death Differ.* **26**, 179–195 (2019).
24. Roman, B. et al. MICU3 regulates mitochondrial calcium and cardiac hypertrophy. *Circ. Res.* **135**, 26–40 (2024).
25. Puente, B. N. et al. MICU3 plays an important role in cardiovascular function. *Circ. Res.* **127**, 1571–1573 (2020).
26. Yang, Y.-F. et al. MICU3 regulates mitochondrial Ca^{2+}-dependent antioxidant response in skeletal muscle aging. *Cell Death Dis.* **12**, 1115 (2021).
27. Xing, Y. et al. Dimerization of MICU proteins controls Ca^{2+} influx through the mitochondrial Ca^{2+} uniporter. *Cell Rep.* **26**, 1203–1212.e1204 (2019).
28. Wu, W. et al. The crystal structure of MICU2 provides insight into Ca^{2+} binding and MICU1-MICU2 heterodimer formation. *EMBO Rep.* **20**, e47488 (2019).
29. Park, J. et al. Structure of the MICU1-MICU2 heterodimer provides insights into the gatekeeping threshold shift. *IUCrJ* **7**, 355–365 (2020).
30. Fan, M. et al. Structure and mechanism of the mitochondrial Ca^{2+} uniporter holocomplex. *Nature* **582**, 129–133 (2020).
31. Wang, Y. et al. Structural insights into the Ca^{2+}-dependent gating of the human mitochondrial calcium uniporter. *Elife* **9**, e60513 (2020).
32. Zhuo, W. et al. Structure of intact human MCU supercomplex with the auxiliary MICU subunits. *Protein Cell* **12**, 220–229 (2021).
33. Paillard, M. et al. MICU1 interacts with the D-ring of the MCU pore to control its Ca^{2+} flux and sensitivity to Ru360. *Mol. Cell* **72**, 778–785.e773 (2018).

34. Phillips, C. B., Tsai, C. W. & Tsai, M. F. The conserved aspartate ring of MCU mediates MICU1 binding and regulation in the mitochondrial calcium uniporter complex. *Elife* **8**, e41112 (2019).
35. Tsai, C.-W. et al. Evidence supporting the MICU1 occlusion mechanism and against the potentiation model in the mitochondrial calcium uniporter complex. *Proc. Natl. Acad. Sci. USA* **120**, e2217665120 (2023).
36. Bick, A. G., Calvo, S. E. & Mootha, V. K. Evolutionary diversity of the mitochondrial calcium uniporter. *Science* **336**, 886 (2012).
37. Pittis, A. A. et al. Discovery of EMRE in fungi resolves the true evolutionary history of the mitochondrial calcium uniporter. *Nat. Commun.* **11**, 4031 (2020).
38. Tsai, M. F. et al. Dual functions of a small regulatory subunit in the mitochondrial calcium uniporter complex. *Elife* **5**, e15545 (2016).
39. Van Keuren, A. M. et al. Mechanisms of EMRE-dependent MCU opening in the mitochondrial calcium uniporter complex. *Cell Rep.* **33**, 108486 (2020).
40. Kovacs-Bogdan, E. et al. Reconstitution of the mitochondrial calcium uniporter in yeast. *Proc. Natl. Acad. Sci. USA* **111**, 8985–8990 (2014).
41. Ghosh, S. et al. An essential role for cardiolipin in the stability and function of the mitochondrial calcium uniporter. *Proc. Natl. Acad. Sci. USA* **117**, 16383–16390 (2020).
42. Yuan, Y. et al. Structural characterization of the N-terminal domain of the Dictyostelium discoideum mitochondrial calcium uniporter. *ACS Omega* **5**, 6452–6460 (2020).
43. Wagner, S. et al. The EF-hand Ca^{2+} binding protein MICU choreographs mitochondrial Ca^{2+} dynamics in Arabidopsis. *Plant Cell* **27**, 3190–3212 (2015).
44. Kamer, K. J., Jiang, W., Kaushik, V. K., Mootha, V. K. & Grabarek, Z. Crystal structure of MICU2 and comparison with MICU1 reveal insights into the uniporter gating mechanism. *Proc. Natl. Acad. Sci. USA* **116**, 3546–3555 (2019).
45. Wu, W. et al. The structure of the MICU1-MICU2 complex unveils the regulation of the mitochondrial calcium uniporter. *EMBO J.* **39**, e104285 (2020).
46. Kamer, K. J. & Mootha, V. K. MICU1 and MICU2 play nonredundant roles in the regulation of the mitochondrial calcium uniporter. *EMBO Rep.* **15**, 299–307 (2014).
47. Gautier, R., Douguet, D., Antonny, B. & Drin, G. HELIQUEST: a web server to screen sequences with specific α-helical properties. *Bioinformatics* **24**, 2101–2102 (2008).
48. Wang, C., Jacewicz, A., Delgado, B. D., Baradaran, R. & Long, S. B. Structures reveal gatekeeping of the mitochondrial Ca^{2+} uniporter by MICU1-MICU2. *Elife* **9**, e59991 (2020).
49. Gottschalk, B. et al. MICU1 controls cristae junction and spatially anchors mitochondrial Ca^{2+} uniporter complex. *Nat. Commun.* **10**, 3732 (2019).
50. Kabsch, W. XDS. *Acta Crystallogr. Sect. D Biol. Crystallogr.* **66**, 125–132 (2010).
51. Otwinowski, Z. & Minor, W. in *Methods in enzymology*, 276, 307–326 (Elsevier, 1997).
52. Liebschner, D. et al. Macromolecular structure determination using X-rays, neutrons and electrons: recent developments in Phenix. *Acta Crystallogr. Sect. D Struct. Biol.* **75**, 861–877 (2019).
53. Emsley, P., Lohkamp, B., Scott, W. G. & Cowtan, K. Features and development of Coot. *Acta Crystallogr. Sect. D Biol. Crystallogr.* **66**, 486–501 (2010).
54. Agirre, J. et al. The CCP4 suite: integrative software for macromolecular crystallography. *Acta Crystallogr. Sect. D Struct. Biol.* **79**, 449–461 (2023).
55. Schrodinger, L. The PyMOL molecular graphics system. *Version* **1**, 8 (2015).
56. Krissinel, E. & Henrick, K. Inference of macromolecular assemblies from crystalline state. *J. Mol. Biol.* **372**, 774–797 (2007).
57. Xue, L. C., Rodrigues, J. P., Kastritis, P. L., Bonvin, A. M. & Vangone, A. PRODIGY: a web server for predicting the binding affinity of protein-protein complexes. *Bioinformatics* **32**, 3676–3678 (2016).
58. Abramson, J. et al. Accurate structure prediction of biomolecular interactions with AlphaFold 3. *Nature*, **636**, e4 (2024).
59. Kumar, S., Stecher, G., Li, M., Knyaz, C. & Tamura, K. MEGA X: molecular evolutionary genetics analysis across computing platforms. *Mol. Biol. Evol.* **35**, 1547–1549 (2018).
60. Robert, X. & Gouet, P. Deciphering key features in protein structures with the new ENDscript server. *Nucleic Acids Res.* **42**, W320–W324 (2014).
61. Sigrist, C. J. et al. New and continuing developments at PROSITE. *Nucleic Acids Res.* **41**, D344–D347 (2012).
62. Ashkenazy, H. et al. ConSurf 2016: an improved methodology to estimate and visualize evolutionary conservation in macromolecules. *Nucleic Acids Res.* **44**, W344–W350 (2016).
63. Duhr, S. & Braun, D. Why molecules move along a temperature gradient. *Proc. Natl. Acad. Sci. USA* **103**, 19678–19682 (2006).
64. Seidel, S. A. et al. Microscale thermophoresis quantifies biomolecular interactions under previously challenging conditions. *Methods* **59**, 301–315 (2013).
65. Park, K. R. et al. Structural implications of Ca^{2+}-dependent actin-bundling function of human EFhd2/Swiprosin-1. *Sci. Rep.* **6**, 39095 (2016).

Acknowledgements

We gratefully acknowledge the staff at beamlines BL-5C and 7A of the Pohang Accelerator Laboratory (Pohang, South Korea) for their invaluable assistance with data collection. We also extend our sincere thanks to Professor Kwang Yeon Hwang (Korea University, Department of Biotechnology) for kindly providing access to essential experimental instruments. This research was supported by the National Research Foundation (NRF) of the Korean government (NRF-2021R1A2C1006267) and by the Bio&Medical Technology Development Program of the National Research Foundation (NRF) funded by the Korean government (RS-2024-00344154 and RS-2024-00440614).

Author contributions

S.H.E. and M.J. conceived the study and organized experiments; M.J. performed most experiments; J.Y., J.P., and H.K. contributed to X-ray diffraction experiments and data analysis. All authors contributed to the interpretation of results and the preparation of the manuscript.

Competing interests

The authors declare no competing interests.

Additional information

Supplementary information The online version contains supplementary material available at https://doi.org/10.1038/s42003-025-08218-1.

Correspondence and requests for materials should be addressed to Soo Hyun Eom.

Peer review information *Communications Biology* thanks Chongyuan Wang and the other, anonymous, reviewers for their contribution to the peer review of this work. Primary Handling Editors: Laura Rodríguez Pérez.